Tutorial

The Fresnel volume and transmitted waves

Jesper Spetzler[*] and Roel Snieder[‡]

ABSTRACT

In seismic imaging experiments, it is common to use a geometric ray theory that is an asymptotic solution of the wave equation in the high-frequency limit. Consequently, it is assumed that waves propagate along infinitely narrow lines through space, called rays, that join the source and receiver. In reality, recorded waves have a finite-frequency content. The band limitation of waves implies that the propagation of waves is extended to a finite volume of space around the geometrical ray path. This volume is called the Fresnel volume. In this tutorial, we introduce the physics of the Fresnel volume and we present a solution of the wave equation that accounts for the band limitation of waves. The finite-frequency wave theory specifies sensitivity kernels that linearly relate the traveltime and amplitude of band-limited transmitted and reflected waves to slowness variations in the earth. The Fresnel zone and the finite-frequency sensitivity kernels are closely connected through the concept of constructive interference of waves. The finite-frequency wave theory leads to the counterintuitive result that a pointlike velocity perturbation placed on the geometric ray in three dimensions does not cause a perturbation of the phase of the wavefield. Also, it turns out that Fermat's theorem in the context of geometric ray theory is a special case of the finite-frequency wave theory in the limit of infinite frequency. Last, we address the misconception that the width of the Fresnel volume limits the resolution in imaging experiments.

INTRODUCTION

In seismic imaging techniques, ray theory is frequently used as the workhorse to construct the forward and inverse wavefield operators in modeling and inversion. The popularity of ray theory is partly due to the limitations in computer power and memory because ray theory is computationally efficient and easy to implement in seismic imaging methods. On the other hand, seismic imaging experiments (Berkhout, 1984; Yilmaz, 1987; Williamson, 1991; Wordward, 1992) have shown clear indications that ray theory, because of its approximate description of wavefield propagation, is inadequate in imaging of media where diffraction effects are important. A comprehensive overview of seismic ray theory is given by Červený (2001).

In seismological experiments, recorded reflection and transmission signals emitted from a broadband source contain mostly low-frequency components because the earth attenuates high-frequency waves. Ray theory, however, is based on a high-frequency approximation. This implies that there may be a methodological conflict between the imaging technique based on ray theory and the measured wavefield. The region around a ray that mostly influences the propagation of a band-limited wave is called the *first Fresnel zone*. Ray theory works well in media with structures that have a length-scale larger than the first Fresnel zone of the recorded wavefield (Sheriff and Geldart, 1982; Berkhout, 1984; Yilmaz, 1987; Williamson, 1991; Williamson and Worthington, 1993; Chen and Schuster, 1999). For low-frequency reflected waves (e.g., frequency contents in the range 10–70 Hz) and transmitted waves (e.g., with frequencies between 300 and 800 Hz), the width of first Fresnel zone can be on the order of 500 m and 50 m, respectively. This width is larger than most of the features that one aims to image in land and marine reflection seismic surveys or in crosswell and vertical seismic profiling (VSP) experiments.

In this tutorial, we show how the seismic resolution limit can be extended to heterogeneous structures with a size smaller than the first Fresnel zone. We show how to generalise the ray theoretical formalism for traveltimes and amplitudes to a more accurate wave theoretical approach that accounts for the band limitation of reflection and transmission signals. The finite-frequency wave theory provides sensitivity kernels (also known as Fréchet kernels) for reflected and transmitted waves.

These finite-frequency Fréchet kernels linearly relate velocity perturbations to changes in traveltime and amplitude. The finite-frequency wave approach is directly applicable to seismic tomographic experiments such as crosswell, VSP, reflection, and migration experiments. The Fréchet kernel naturally connects to the Fresnel zone because both concepts are derived using the idea of constructive interference of waves.

This tutorial has the following structure. Starting from the Kirchhoff integral, we formulate the concept of Fresnel zones in a homogeneous medium. Next, the sensitivity kernel for finite-frequency waves in a homogeneous medium is introduced. Then, an example of the breakdown of ray theory is illustrated. Afterwards, we extend the formalism for Fresnel zones and Fréchet kernels to heterogeneous media, and we show several examples of high-resolution seismic experiments wherein the resolution is not limited to the first Fresnel zone.

THE FRESNEL VOLUME

In ray theory, waves propagate along rays that form a line or several lines connecting the source to the receiver. In reality, a wave does not strictly propagate along a line. A wave is a collective phenomenon in which the particle motion is organized over a finite region of space (Scales and Snieder, 1999). For waves with a finite-frequency band, discontinuities in the wavefield tend to be smoothed out as the waves propagate. Hence, the wavefield is continuous over a limited area of propagation. The size of the region over which the wavefield varies is given by the wavelength, which decreases for increasing frequency. This is the physical reason that ray theory is progressively more accurate with increasing frequency.

For finite-frequency wave propagation, the propagation path extends to the tubelike volumes that straddle the rays running from a source to a receiver. In ray theory, these volumes are collapsed into one line (the ray) by the employed infinite-frequency approximation. Here, we follow Kravtsov (1988) and use the Kirchhoff integral to derive the region of space through which the waves travel for a given source-receiver pair.

In Figure 1, a source at location $\mathbf{r}_s$ excites waves. The representation theorem says that the wavefield recorded at the receiver location $\mathbf{r}_r$ can be represented as an integral over a surface S that is placed between the source and receiver. Using the geometry shown in Figure 1, the wavefield at the receiver location can be written as

$$p(\mathbf{r}_r) = \int_S \frac{1}{\rho(\mathbf{r})} (p(\mathbf{r})\nabla G(\mathbf{r}, \mathbf{r}_r) - G(\mathbf{r}, \mathbf{r}_r)\nabla p(\mathbf{r})) \cdot d\mathbf{S},$$

(1)

where $p(\mathbf{r}_r)$ is the acoustic pressure at the receiver position $\mathbf{r}_r$, ρ denotes the mass density and $G(\mathbf{r}, \mathbf{r}_r)$ is the Green's function.
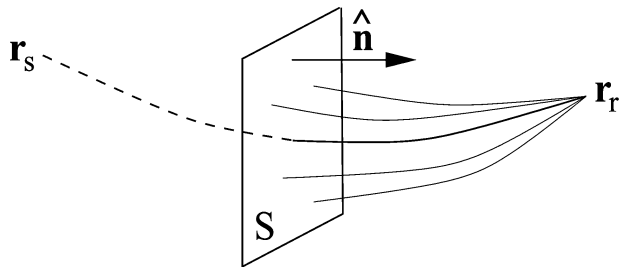
This expression holds for acoustic waves; its derivation can be found in Morse and Feshbach (1953) and in Snieder (2001). The medium for which the Green's function $G(\mathbf{r}, \mathbf{r}_r)$ is defined can be either homogeneous or inhomogeneous. For elastic waves, a similar expression is known under the name of Betti's theorem (Aki and Richards, 1980). Since the mathematical complexity resulting from the tensor character of elastic waves obscures the underlying ideas, we proceed with the representation theorem of equation (1) for acoustic waves. The wavefield on the surface S in the integral (1) is the total wavefield. However, when backscattering is weak, the wavefield in the integral can be replaced by the incident waves that travel directly from the source to the surface S. This is called the *Kirchhoff approximation*.

In the Kirchhoff approximation, the integral (1) can be interpreted as a superposition of waves that have been scattered from different points on the surface S; the associated wave paths are indicated in Figure 1 with thin solid lines. The waves that propagate from points on S close to the geometric ray arrive almost in phase with the primary arrival (i.e., the direct wave). The waves that are radiated from points far from the geometric ray arrive much later than the direct arrival. For this reason, the main contribution to the transmitted wave in integral (1) comes from points on the surface S that are close to the geometric ray. This argument, however, does not tell us yet what "close" means. We make this more specific by considering in the next section the special case of a homogeneous medium.

Example: A homogeneous medium

For a homogeneous model, the geometry of the diffraction process is shown in Figure 2. The incident wave (with wavefronts drawn with solid gray lines) radiates from the source at $\mathbf{r}_s$ to the point $\mathbf{r}$, and gives rise to a diffracted wavefield (with wavefronts drawn with dashed grey lines) that propagates towards the receiver at $\mathbf{r}_r$. The point $\mathbf{r}$ lies on the integration surface S of the expression in equation (1) at a distance x from the source, measured along the geometric ray. The perpendicular distance from the integration point to the geometric ray is denoted by q, and the source-receiver distance is given by L. The detour of the diffracted wave that travelled from the source at $\mathbf{r}_s$ via the integration point $\mathbf{r}$ to the receiver at $\mathbf{r}_r$ is then compared to the length of the geometric ray.

We consider the path-length difference D between the geometric ray with the propagation length equal to the source-receiver distance and the diffracted wave that travels the

Figure 1. The wavefield at the receiver location $\mathbf{r}_r$ expressed as an integral over the surface S.
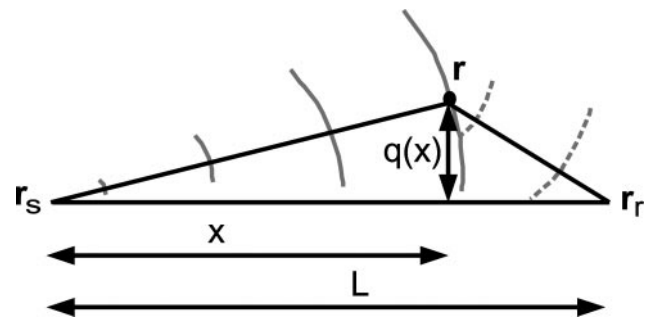

Figure 2. Definition of the geometric variables in a homogeneous velocity model. Wavefronts of the wavefield emitted from the source and the wavefronts of the diffracted wavefield due to the diffractor at position $\mathbf{r}$ are illustrated with the solid and dashed gray lines, respectively.

detoured path from the source at $\mathbf{r}_s$ via the integration point $\mathbf{r}$ to the receiver at $\mathbf{r}_r$. The path-length difference of the detour and direct ray is given by

$$D = \sqrt{x^2 + q^2(x)} + \sqrt{(L-x)^2 + q^2(x)} - L. \qquad (2)$$

When the deflection $q(x)$ is much smaller than x and $L-x$, a first-order Taylor expansion in q^2 gives the following expression for the detour:

$$D \approx \frac{1}{2}\left(\frac{1}{x} + \frac{1}{L-x}\right)q^2(x). \qquad (3)$$

The wave passing through the diffraction point $\mathbf{r}$ interferes constructively with the direct wave when the path-length difference is small compared to the wavelength λ. The main contribution from the scattering integral in equation (1), therefore, comes from points satisfying the requirement that

$$D < \lambda/n. \qquad (4)$$

The number n denotes the fraction of the wavelength that is allowable for the detour to still provide constructive interference of waves. In the next section, we show analytically that in two dimensions the value $n = 8/3$ is appropriate, whereas in three dimensions $n = 2$. By using the value of n for wave propagation in two dimensions in the equation (4) combined with equation (3), the following condition for constructive interference is derived:

$$q(x) < \sqrt{\frac{3}{4}\frac{\lambda x(L-x)}{L}}. \qquad (5)$$

This condition defines the central white area shown in Figure 3, which illustrates the first six Fresnel zones in a homogeneous 2D medium. The first, third, and fifth Fresnel zones correspond to detours that give constructive interference (the white areas), whereas the second, fourth and sixth Fresnel zones imply detours that yield destructive interference (the black regions). It is clear from Figure 3 that the most important area is the first Fresnel zone, which generates diffracted waves that interfere constructively with the direct arrival. Hence, a velocity perturbation of the medium affects the direct wave when this perturbation is located inside the first Fresnel zone.

In contrast to the first Fresnel zone, the higher order Fresnel zones alter rapidly between positive and negative wavefield interference so that the total response from the higher order Fresnel zones to the wavefield recorded at the receiver cancels out upon integration over the surface S. Here, the first Fresnel zone is simply referred to as the Fresnel zone, or alternatively as the Fresnel volume (Červený and Soares, 1992).

FINITE-FREQUENCY FRÉCHET KERNELS IN A HOMOGENEOUS MEDIUM

The Fresnel volume is based on the concept of constructive inference of scattered waves with respect to the geometric
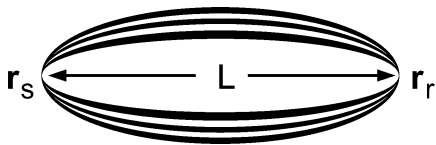

Figure 3. The first six Fresnel volumes for a homogeneous velocity model.

arrival. This may suggest that the Fresnel volume has a sharp cutoff, and that the sensitivity of the wavefield to perturbations of the medium is uniform within the Fresnel zone. However, the continuity of the wavefield ensures that the related sensitivity has a gradual rather than a sharp cutoff. In Appendix A, we study this cutoff by showing a derivation of the Kirchhoff integral and the sensitivity kernels of the wavefield as functions of the slowness perturbation field. Here, we continue the treatment of the Fresnel volume by using the sensitivity kernels as an indicator for the shape of the Fresnel volume.

The sensitivity of the phase and amplitude of wavefields is extracted from the sensitivity kernel, also known as the Fréchet kernel (Tarantola, 1987), which is a function of the wavelength, the velocity, and the positions of the source and receiver. The Fréchet kernel for phase and amplitude variations can be derived from the first-order Rytov approximation (e.g., Aki and Richards, 1980; Snieder and Lomax, 1996; Spetzler and Snieder, 2001), which accounts for the first-order perturbation of the phase and amplitude of waves. In general, the perturbation of phase and amplitude is an integral of the sensitivity kernel $K(\mathbf{r})$ multiplied by the slowness perturbation field $\delta u(\mathbf{r})$ [or the velocity perturbation field $\delta v(\mathbf{r})$] over the volume between the source and receiver. For instance, the traveltime variation δt due to scattering and diffraction phenomena can be written as

$$\delta t = \int_V K(\mathbf{r})\delta u(\mathbf{r})dV. \qquad (6)$$

For the geometry in Figure 2, the sensitivity kernel for a point source in a 2D constant reference-velocity field v_0 is given by

$$K^{2D}(x,z) = \sqrt{\frac{L}{v_0}}\int_{v_0-\Delta v}^{v_0+\Delta v} A(v)\sqrt{v}$$
$$\times \frac{\sin\left(\frac{\pi v L}{v_0}\frac{z^2}{x(L-x)} + \frac{\pi}{4}\right)}{\sqrt{x(L-x)}}dv, \qquad (7)$$

where x is the distance along the reference ray, z is the distance perpendicular to the ray path, L is the propagation distance of the primary arrival and v denotes frequency. The integration over the frequency band $[v_0 - \Delta v; v_0 + \Delta v]$ indicates a band-limited wavefield. The function $A(v)$ is the normalized amplitude spectrum of the recorded wavefield using the normalization condition $\int_{v_0-\Delta v}^{v_0+\Delta v} A(v)dv = 1$. In three dimensions, the Fréchet kernel for a point source in a homogeneous background medium is given by

$$K^{3D}(x,y,z) = \frac{L}{v_0}\int_{v_0-\Delta v}^{v_0+\Delta v} A(v)v\frac{\sin\left(\frac{\pi v L}{v_0}\frac{y^2+z^2}{x(L-x)}\right)}{x(L-x)}dv. \qquad (8)$$

The distance perpendicular to the ray path is equal to $\sqrt{y^2+z^2}$ in three dimensions. Spetzler and Snieder (2001) give a detailed derivation of the sensitivity kernels in equations (7) and (8).

An example of a 2D Fréchet kernel for the traveltime delay of a transmitted wave is illustrated in Figure 4a. The grayscale indicates the sensitivity of the arrival time of a band-limited wave to slowness perturbations throughout the medium. The source wavelet contains frequencies ranging from
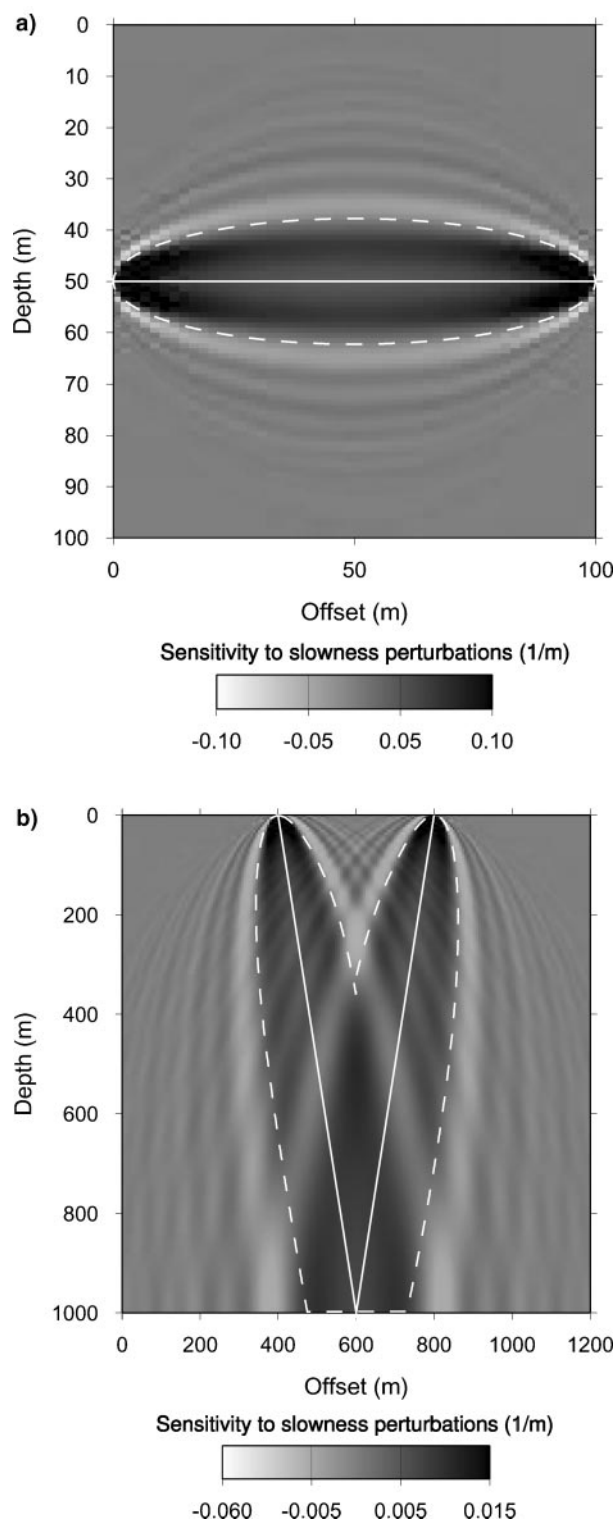
Figure 4. Finite-frequency traveltime delay Fréchet kernels for a transmitted and reflected wave in a homogeneous medium. The ray path between the source and receiver is shown with the white line, and the Fresnel zone boundary for the central frequency is plotted with the white dashed line. (a) Fréchet kernels for a transmitted wave. The constant reference velocity equals 4 km/s, the source-receiver distance is $L = 100$ m, and the frequency range is between 250 and 750 Hz. (b) Fréchet kernels for a reflected wave. The velocity is 4 km/s above the reflecting interface at 1 km. The two-way ray path distance L is equal to 2 km, and the frequency is between 40 and 60 Hz.

250 to 750 Hz, which is representative for borehole-to-borehole and VSP experiments. Because of the homogeneous background velocity, the geometric ray path (solid line) is a straight line and the first Fresnel zone for the central frequency at 500 Hz (dashed line) has the form of an ellipse [except near the source and receiver where the approximate Fresnel zone equation in equation (5) is not accurate]. Notice that the width of the Fresnel zone is as large as 25 m in this experimental geometry, which is several times larger than the central wavelength $\lambda = 8$ m. The sidelobes of the Fréchet kernel in Figure 4a cancel out due to destructive interference of the sensitivity kernel at higher-order Fresnel zones when integrating over a broad frequency band.

This cancellation is explicitly demonstrated in Figure 5a which shows cross-sections of the Fréchet kernel in Figure 4a for different frequencies as a function of the distance perpendicular to the geometric ray. The values for the reference velocity, frequency, and distance from the source to the receiver are the same as in Figure 4a. The curves with the thin solid line are computed for a single-frequency component starting from 250 Hz and increasing in steps of 100 Hz to 750 Hz. Adding the
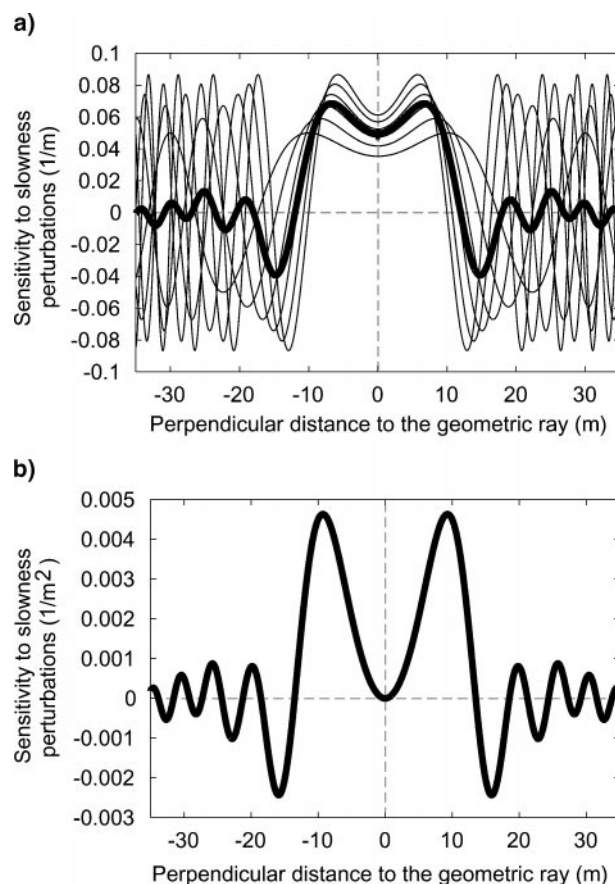

Figure 5. Cross-sections of transmission Fréchet kernels for 2D and 3D wave experiments. The cross-sections are obtained at the halfway between the source and receiver, where the width of the Fresnel zone is largest. (a) Cross-sections (single frequency, thin solid line; frequency averaged, thick solid line) for a 2D Fréchet kernel. The maximum sensitivity to slowness perturbations is away from the ray path. (b) Cross-section for a 3D frequency-averaged Fréchet kernel. Notice the zero sensitivity to the slowness perturbation field on the geometric ray.

single-frequency cross-sections gives the broadband Fréchet kernel in Figure 5a indicated with a thick solid line.

We show in Figure 5b, the cross-section of a broadband sensitivity kernel for timeshifts of transmitted waves propagating in three dimensions. The values for the reference velocity, frequency, and distance from the source to the receiver are identical to those applied in Figure 4a. In both plots of Figure 5, it is clear that the sensitivity to slowness perturbations is greatest away from the geometric ray. The 3D Fréchet kernel actually vanishes on the ray path, which was also observed by Woodward (1992). Physically speaking, this implies that in three dimensions a velocity perturbation placed on the geometric ray does not alter the arrival time of a wave. Fermat's theorem, which is a corollary of ray theory, states that the perturbation of the arrival time is given by the line integral of the slowness perturbation along the geometric ray (Aldridge, 1994). Ray theory thus predicts a nonzero sensitivity to slowness perturbations on the geometric ray. This phenomenon has recently been called the *banana-doughnut paradox* by Marquering et al. (1999).

At first glance, it may seem that there is a contradiction between ray theory and the finite-frequency wave theory. The apparently conflicting sensitivities of ray theory and wave theory for slowness perturbations on the geometric ray can be reconciled when the slowness perturbation has a geometric size greater than the width of the Fresnel volume. In that case, the requirements for ray theory are valid. One can then show analytically with the stationary phase approximation that the band-limited traveltime perturbation of equation (6) gives the same traveltime perturbations as predicted by ray theory (Spetzler and Snieder, 2001; Dahlen and Baig, 2002). However, for a slowness perturbation with a size much smaller than the width of the Fresnel volume, the conditions for applying ray theory are not satisfied. In this case, wave theory predicts that in three dimensions the slowness perturbation does not alter the arrival time when the perturbation is located on the geometric ray.

The Fréchet kernel for wave propagation in a 2D homogeneous medium given in equation (7) has its first zero crossing near the reference ray when the argument of the sine function equals π, thus $\pi \nu L z^2 / (v_0 x (L - x)) + \pi/4 = \pi$. Equating z in this equation with the distance q in expression (3) gives the detour's path length difference D to be equal to $3\lambda/8$ at the first zero crossing of the Fréchet derivative. Hence, the value of $n = 8/3$ for constructive interference of waves as mentioned earlier. A similar analysis for the 3D Fréchet kernel in equation (8) gives $D = \lambda/2$ for the zero crossing of the Fréchet kernel. Thus in three dimensions, $n = 2$.

The formalism for the Fréchet kernels of phase and amplitude variations of wavefields can be extended to reflected waves. According to one-way wave theory (e.g., Wapenaar and Herrmann, 1996), reflected waves can be decomposed into a downgoing wavefield from the source to the reflector and an upgoing wavefield from the reflector to the receiver. Accordingly, the sensitivity kernel for the timeshift of a reflected wave can be obtained from the composition of two Fréchet kernels: one sensitivity kernel for the downward propagating wavefield and another Fréchet kernel for the upward propagating wavefield. An example of the sensitivity kernel for a reflected wave is illustrated in Figure 4b. In this case, the width of the Fresnel volume at the reflector of depth 1 km is on the order of 400 m ($\lambda = 100$ m and the two-way path length L is 2-km long).

This is four times the wavelength and a fifth of the two-way path length. This example shows that the width of the Fresnel volume can be large for realistic wave experiments in exploration seismology. Similar estimates of the Fresnel volume width for reflected waves can be found in Sheriff and Geldart (1982), Berkhout (1984), Knapp (1991), Hubral et al. (1993), and Schleicher et al. (1997).

We return to the sensitivity kernel for the relative amplitude variations of finite-frequency waves. According to Aki and Richards (1980), the Fréchet kernel $K(\mathbf{r})$ for the relative amplitude perturbation $\delta A / A$ is given by expression (7) for two dimensions or by expression (8) for three dimensions where the sine function is replaced by a cosine. Plots of sensitivity kernels for amplitude perturbations can be found in Aki and Richards (1980) and Snieder and Lomax (1996). In seismic experiments, the amplitude information has a larger uncertainty than the phase information. The amplitude of a recorded wavefield is influenced by several other factors that include attenuation due to energy losses, geometrical spreading, source and receiver coupling, and directivity (e.g. Williamson, 1991). In the remaining part of this tutorial, we focus on seismic imaging techniques that use phase information only as data input.

Gaussian beam theory represents an alternative approach to extend the sensitivity of propagating waves to a finite volume around the geometric ray (Červený, 2001). This theory proposes that high-frequency wavefields propagate along the ray path between the source and receiver. The amplitude along the wavefront decays as a Gaussian function away from the ray path. One major difference between Gaussian beam theory and the finite-frequency wave theory is in the prediction of the traveltime sensitivity on the ray path. Gaussian beam theory predicts maximum sensitivity on the geometric ray, whereas the scattering theory presented for finite-frequency waves prescribes a minimum sensitivity on the ray for 2D and 3D media. In addition, the width of the Gaussian beam needs to prescribed in an ad hoc fashion, whereas the theory presented here is self-consistent in the sense that it does not require any additional parameters.

RAY THEORY AND FINITE-FREQUENCY WAVE THEORY REGIME EXAMPLE

In Figure 6, we present a comparison of ray theory and scattering theory with a finite-difference solution of the wave equation. A horizontally propagating plane wave is incident from the left, and a vertical receiver line is placed at 100 m offset. The slowness perturbation (grayscale) has fluctuations with a length scale that decreases with depth. The strength of the velocity perturbation field is 2.5% relative to the constant reference-velocity field of 4 km/s. The central frequency of the plane wave is 200 Hz. The average width of the Fresnel zone for plane waves is approximately 65 m at the position of the heterogeneous slab. The width of the Fresnel volume is smaller in size than the characteristic length scale of velocity anomalies above 250 m depth, while below this depth the length scale of the slowness variations is less than the width of the Fresnel volume. This implies that the conditions for the validity of ray theory are satisfied only in the top part of Figure 6 down to 250 m. For depths below 250 m, the length scale of the slowness perturbation is so small that ray theory is not valid. The jagged

line at 250 m depth represents the transition zone between the regimes of ray theory and scattering theory.

The "true" delay time of the waves was determined by creating synthetic seismograms using a finite-difference scheme for a homogeneous model and for a model including the slab of slowness perturbations. The difference in the arrival time of these modeled waveforms in the two models gives an estimate of the "true" perturbation in the arrival time. This delay time is indicated with a red line. The delay time predicted by ray theory is shown with a yellow line, whereas the time shift computed with scattering theory using expression (6) is shown with a blue line. Both ray theory and scattering theory do well in predicting the delay time from the finite-difference modelling for depths less than 250 m, where ray theory is valid. For greater depths, only scattering theory is capable of estimating the correct value of the timeshift. At these depths, the delay times computed with ray theory are too large in magnitude compared to the traveltime shifts determined from the finite-difference synthetics. At several depths, the ray-theoretical traveltime delays are anticorrelated with the observed ones. If these delay times were to be inverted with a ray-geometrical tomographic algorithm, the inferred slowness perturbations would have the wrong sign.
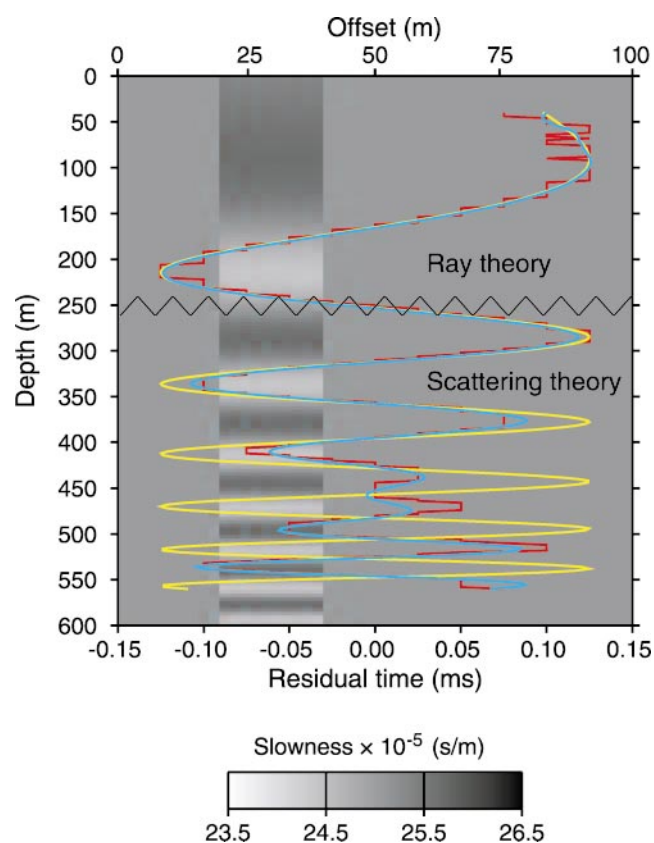

Figure 6. Synthetic test of the scattering theoretical approach using a plane incoming wave that propagates through a medium with small-scale structure. The perturbed slowness field is shown in grayscale. The timeshifts retrieved from the finite-difference computation are indicated with a red line, and the residual times computed with ray theory and scattering theory are shown in yellow and blue, respectively. The horizontal, jagged line separates the regime of ray theory from that of scattering theory.

Notice that the strength (i.e., 2.5%) of the velocity perturbations in the synthetic transmission experiment in Figure 6 are smaller than the values of the velocity perturbation strength observed in typical seismic transmission experiments, where the velocity perturbations can be as large as 10–15%. However, if the breakdown of ray theory for finite-frequency waves is significant in a weakly perturbed velocity field, this complication will certainly be important in heterogeneous media with a larger strength of velocity perturbations. Examples of finite-frequency transmission experiments using a more complex velocity perturbation field with a strength of 10% compared to the reference medium are shown in Spetzler et al. (2002), Spetzler (2003), and in the next sections.

FRESNEL VOLUMES AND FRÉCHET KERNELS IN HETEROGENEOUS MEDIA

The theory for Fresnel volumes and finite-frequency waves can be extended to heterogeneous reference media. Efficient methods for computing Fresnel volumes have been formulated using either expressions for the wavefront curvature (Červený and Soares, 1992) or a formulation based on paraxial rays (Pulliam and Snieder, 1998). Snieder and Lomax (1996) and Snieder and Chapman (1998) generalise the finite-frequency wave theory to heterogeneous background models by taking the wavefront curvature and geometrical spreading factor for curved rays into account.

An example of two 2D finite-frequency Fréchet kernels for traveltime delays of transmitted waves in a reference medium with a constant velocity gradient is presented in Figure 7. The frequency content is between 250 and 750 Hz, the source-receiver distance is on the order of 100 m, and the velocity varies linearly with depth with $v(z = 0$ m$) = 3.5$ km/s and $v(z = 150$ m$) = 5$ km/s. This example is relevant for crosswell and VSP tomography. The rays joining the source and receiver are indicated with the solid white lines, and the Fresnel zone for the central frequency at 500 Hz is illustrated with the dashed white lines. To reduce the computation time of the band-limited Fréchet kernels, the volume integration in equation (6) is truncated to a higher Fresnel zone (i.e., dashed black lines). The grayscale colors indicate the sensitivity of the broadband waves to slowness perturbations for the two source-receiver pairs. Notice that the Fréchet kernels bend towards larger depths since the reference velocity increases with depth.

The finite-frequency Fréchet kernels for heterogeneous reference media have been validated in the numerical finite-difference experiment similar to the one in Figure 6. The result of a numerical modeling experiment is shown in Figure 8a. We apply the same colour convention for the finite-difference scheme and ray-theoretical and finite-frequency predicted timeshifts as in Figure 6. The velocity model (the grayscale color) consists of a large-scale and a small-scale structure. For the heterogeneous large-scale structure, we use the linear gradient medium as in Figure 7 combined with two negative small-scale velocity perturbations with a strength of 8% at depths about 68 m and 83 m. The vertical characteristic length (i.e., 5 m) of the two anomalies is much smaller that the Fresnel zone of the transmitted waves (i.e., 25 m), hence the requirements for ray theory are invalid in this velocity model. From the three curves of the travel timeshift in Figure 8a, it is clear that only the finite-frequency wave theory predicts well the

finite-difference traveltime delays. Interestingly, we see that the finite-frequency timeshift curves have one maximum instead of two peaks, which is the case for the ray-theoretical time delay curve. An interpretation based on ray theory of the "observed" travel timeshifts would lead to the idea of one velocity anomaly only, but in fact there are two small-scale velocity perturbations present in the velocity model.

To show the effect of focusing-defocussing effects, we have used a shooting method to trace rays with different incident angles from the source depth at 75 m in Figure 8b. We clearly see that two foci (related to caustics and triplications) are present at the 60–80 m offset range. In the vertical section between the foci, the rays are sparse because of defocusing. In general, the effect of focusing and defocussing complicates an estimation of traveltimes. The example in Figure 8b illustrates that the linear finite-frequency wave theory in this case explains the arrival time very well, despite the severe ray bending and focusing that is caused by the velocity anomalies.

Figure 9 shows a remarkable example of a Fresnel zone with a complicated shape. The example is from global seismology, and shows the Fresnel zone projected on the earth's surface of a PP-wave arrival with the epicentral distance of 107°. Such
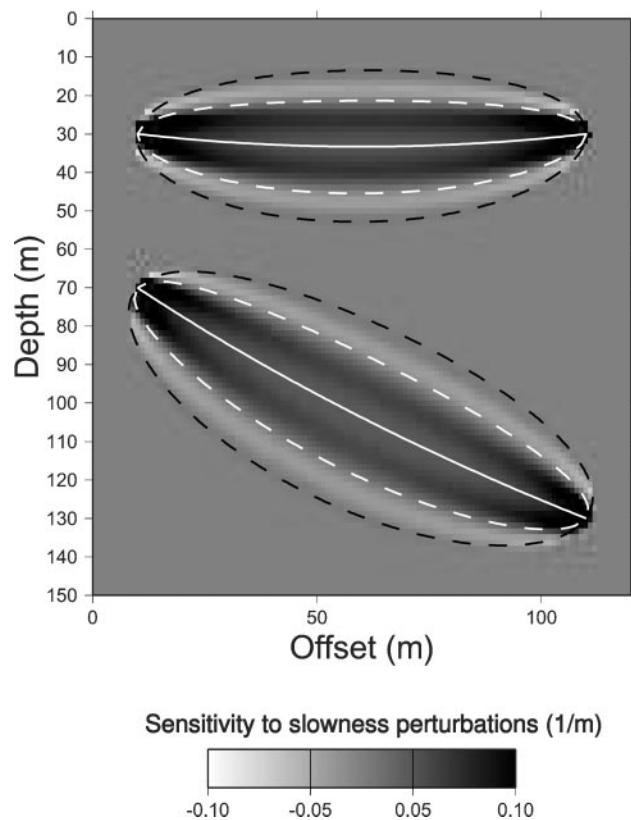

Figure 7. Sensitivity kernels for band-limited transmitted wavefields with different source-receiver positions in a heterogeneous reference slowness field. The background model is a constant velocity gradient medium having the velocity 3 km/s at 0-m depth and 5 km/s at 150-m depth. The frequency of the wavefield is in the range from 250 to 750 Hz. The white solid line indicates the ray path between the source and receiver, the white dashed line shows the Fresnel zone boundary, and the dashed black line refers to the truncated volume for the integration in equation (6).

an event is called a minimax phase because the traveltime *decreases* when the surface coordinate of the wave is moved away from the specular reflection point (at 0° latitude and 53.5° longitude) along the source-receiver line (i.e., aligned to 0° latitude), whereas the traveltime *increases* when the surface coordinate is moved perpendicular to the source-receiver line. The Fresnel zone of the PP-wave at the surface of the earth has a hyperbolic shape with thin arms that extend far from the geometric ray (e.g., Kravtsov, 1988; Neele and Snieder, 1992).

HIGH-RESOLUTION SEISMIC IMAGING EXPERIMENTS

We present two examples of high-resolution experiments that are relevant for exploration seismology. In both experiments, the heterogeneous velocity models have structures with a length scale that is smaller in size than the Fresnel volume of the recorded wavefield. The first example is a crosswell tomographic inversion of traveltime shifts from broadband transmission signals, and the second example is a migration experiment.

The "observed" traveltime delays in the borehole-to-borehole inversion experiment are computed with equation (6), and the velocity structure in Figure 8 is the true velocity model. The frequency content of the wavefield ranges between 250 and 750 Hz. The vertical line of sources is located at 0-m offset, while the vertical receiver line is at 100-m offset. There are 101 sources and receivers between the depths of 25 and 125 m, with a separation of 1 m; thus in total the data set consists of 10 201 traveltime perturbations. The presented crosswell experiment is similar to the experiments of Pratt and Coulty (1991) and Reiter and Rodi (1996). We use an ordinary least-squares inversion to invert the synthetic data using sensitivity kernels compiled with the finite-frequency wave theory and the ray theory. In Figure 10, the true velocity model (a) and the inverted velocity models inferred from diffraction theory (b) and ray theory (c) are shown. It is clear from this synthetic experiment that the inversion based on scattering theory reproduces the true velocity model well. In contrast, the inverted velocity model from the ray theoretical inversion shows an indication of one anomaly only located at a depth of about 70–75 m. This spurious anomaly is located in between the two true velocity perturbations. For a recent example of finite-frequency crosswell tomography using ultrasonic broadband waveform data in a laboratory experiment, see Spetzler (2003).

The issue of resolution in migration experiments has been studied both analytically and numerically. Berkhout (1984) and Chen and Schuster (1999) formulate criteria for the horizontal resolution limit, which depends on parameters such as aperture, diffractor depth, and wavenumber. Berkhout (1984) and Yilmaz (1987) show synthetic examples of high-resolution migration experiments using reflection models with significant small-scale structure. Following Berkhout (1984) and Yilmaz (1987), we illustrate with a synthetic migration experiment in Figure 11 that it is possible to obtain a clear image of reflecting interfaces with a horizontal length scale that is much smaller than the width of the Fresnel volume at the reflector. The synthetic migration experiment employs band-limited zero-offset data with a central frequency of 50 Hz. The input-model consists of six reflectors with decreasing horizontal extent (indicated with closed solid lines) at 1-km depth. The horizontal extent of the reflectors is 400, 250, 75, 25, 15, and 5 m. The reference velocity field is 4 km/s everywhere, so the width of the

Fresnel volume at the reflectors is approximately 400 m. The Fresnel volumes for three different source positions are shown with three semiellipses in Figure 11. To account for the band limitation of the waves in the migration experiment, we used a 45° finite-difference migration scheme for zero-offset data to simulate the wave propagation (Claerbout, 1984; Stockwell, 1997). The grayscale in Figure 11 shows the migrated model. Reflectors with the horizontal extent as small as 25 m are clearly seen, while the two smallest reflectors are nearly or completely invisible. Notice that the horizontal resolution in this synthetic migration experiment is much smaller than the width of the Fresnel zone.

Another interesting example of a high-resolution experiment closely connected to migration is synthetic aperture radar (SAR) (e.g., Bamler and Hartl, 1998; Massonnet and Feigl, 1998). SAR is usually used from satellites that circle the Earth, but this technique has also been employed using radar systems mounted in aircraft. These satellites emit radar waves that are reflected at the earth's surface and are recorded by the satellite. Thus, SAR has a close analogy to reflection seismic experiments. Within the earth sciences, SAR is mostly used to create high-resolution images of topography. In SAR applications from space, the highest resolution is on the order of 100 m while the footprint of the radar beam is a factor 25 times larger in size (about 2.5 km). Both migration techniques and SAR combine the information acquired in many different shot-receivers combinations to unscramble the averaging that has occurred in the reflection of a wave for a single shot-receiver geometry. The example shown in Figure 11 shows that seismic migration indeed carries out this process and that the resolution of the final image is not limited by the width of the Fresnel zone.

DISCUSSION

The concept of the Fresnel volume and the sensitivity kernels that account for the influence of small-scale velocity perturbations on the traveltime of waves serve not only to provide a better understanding of wave propagation. This theory can also be used in a number of ways in seismic imaging. The integral in equation (6) provides a simple expression for the leading order perturbation in the arrival time of waves caused by small-scale velocity perturbations. It also can be used to compute the effective velocity of waves propagating through media with small-scale velocity perturbations.

In migration, one needs to compute the wavefield propagators that specify how waves propagate from the source to reflection points in the subsurface and from there to the receivers. In applications where one wants to account for the imprint of small-scale velocity perturbation on the wave propagation operators used in migration, one can use expression (6) for computing the imprint of these small-scale velocity perturbations on the phase propagators.

An important application of the theory presented here is transmission tomography, which is relevant in cross-borehole tomography and VSP experiments. In many applications, transmission tomography is based on geometric ray theory. In that
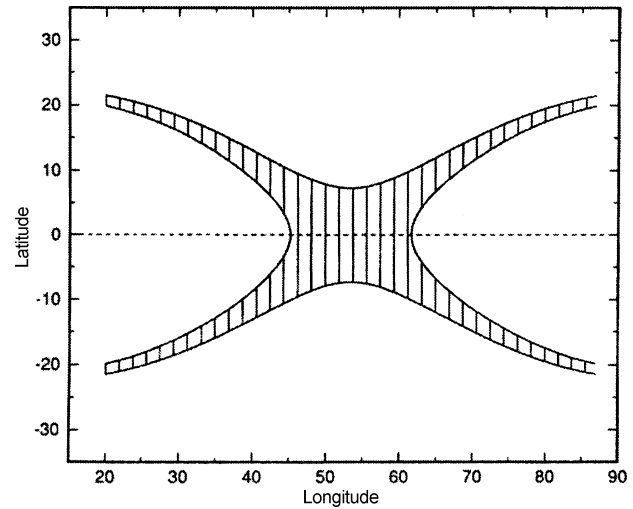

Figure 9. The Fresnel volume (shaded) for a PP-wave at its bounce point for an epicentral distance of 107° and a period of 20 s. The source-receiver direction is indicated with the dashed line at 0° latitude.

Figure 8. Validation of the finite-frequency Fréchet kernels in Figure 7 using a synthetic forward modelling experiment. The "true" velocity medium is a combination of a heterogeneous reference medium and two small-scale anomalies located at depths 68 m and 83 m, respectively. (a) Finite-difference experiment as in Figure 6 using the wavefield modelling parameters in Figure 7. The colour convention for the travel timeshifts is the same as in Figure 6. (b) A ray-path shooting experiment showing that nonlinear defocusing effects are operative in the wavefield modelling experiment.
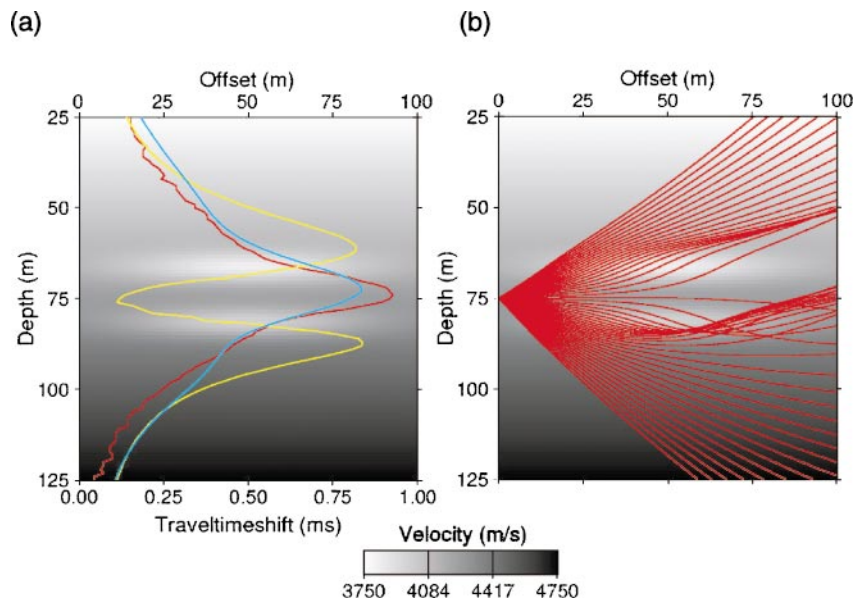
context, the well-known Fermat's theorem states that the traveltime perturbation is given by the line integration of the slowness perturbation along the reference ray. The application of Fermat's theorem is unjustified when the velocity perturbations have a size smaller than the width of the Fresnel volume. In that situation, expression (6) can be used as a basis for a linear inversion scheme, as illustrated with the borehole-to-borehole experiment in Figure 10. Because of its linear character, it is as easy to implement the finite-frequency wave theory stated in equation (6) as the ray-geometric line integral in tomographic inversions.

The Rytov approximation can also be used as the basis for diffraction tomography. This approach was taken by Yomogida and Aki (1987), who inverted surface wave data for the structure under the Pacific Ocean. Woodward (1992) used a similar technique for the analysis of seismic reflection data. In general, the theory presented here seems most useful for the analysis of transmission data and for the computation of the Green's functions that are needed for imaging seismic reflection data in the presence of small-scale velocity variations.

The theory presented here relies on the linearized relationship between the small-scale velocity perturbations and the perturbation of the phase and amplitude of the waves. In reality, higher order perturbations of the phase may also be important. Within the context of geometric ray theory, ray bending leads to a second-order relation between the arrival time and the slowness perturbation (Snieder and Sambridge, 1992). Another nonlinear phenomenon is wavefront healing, wherein the diffraction of waves around velocity perturbations leads to a different imprint of fast velocity anomalies on the wavefronts than slow velocity anomalies (Wielandt, 1987; Nolet and Dahlen, 2000). The theory presented here does not account for the nonlinearity due to ray bending and wavefront healing, and one should be aware that these mechanisms may be operative in strongly heterogeneous media. The theory presented here nevertheless does account for the first-order imprint of the velocity perturbation on the propagation of seismic waves.
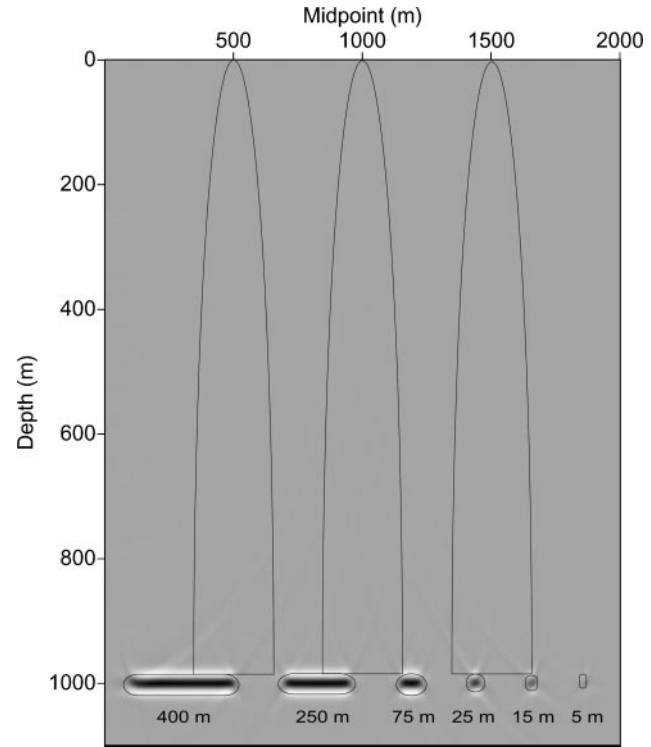
Figure 11. A migration experiment using zero-offset data. The reflectors are shown with the rectangles at 1-km depth. The length of the reflectors decreases from 400 to 5 m. The width of the Fresnel volume at 1-km depth is approximately 400 m. The semi-ellipses represent the Fresnel volume for zero-offset waves at different source-receiver positions.
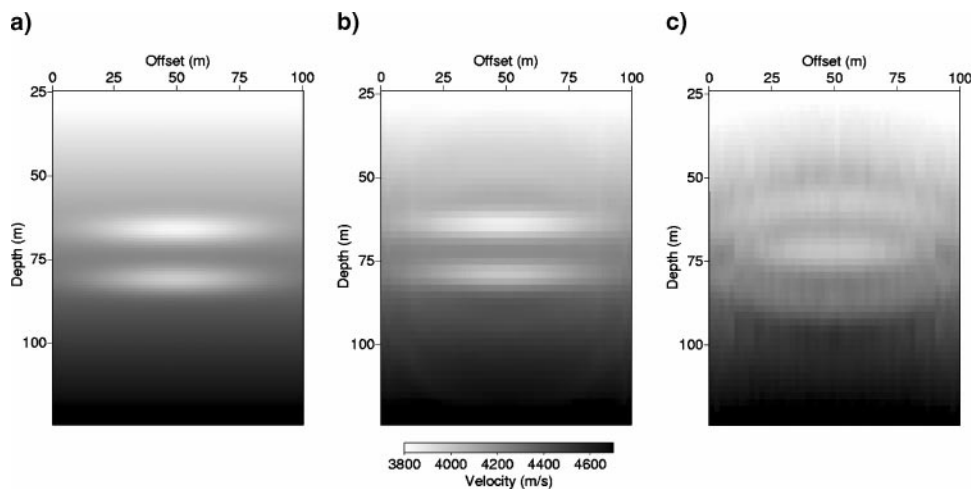

Figure 10. Finite-frequency borehole-to-borehole inversion experiment. (a) The true velocity model is the same as in Figure 8. (b) The inverted velocity using finite-frequency wave theory. (c) The inverted velocity compiled with ray theory.

Methods for Complex Structures at the Center for Wave Phenomena. Figure 11 was created with the Seismic Unix software package from Colorado School of Mines (Stockwell, 1997). We are additionally grateful to Kees Wapenaar and Ken Larner for their constructive comments on the manuscript. The two reviewers Bob Sheriff and Li-Yun Fu and Editor Gerard Schuster interfered constructively to the original manuscript which helped us to improve its large-scale, as well as, small-scale structure.

APPENDIX A

THE RELATIONSHIP BETWEEN THE KIRCHHOFF INTEGRAL AND THE FRÉCHET KERNEL

In this appendix, we show how the Kirchhoff integral is connected to the finite-frequency sensitivity kernel. The starting point of the derivation is the Kirchhoff integral (1) for the calculation of the recorded wavefield that propagates through the surface S of diffractor points as illustrated in Figure 1.

When the diffraction point $\mathbf{r}$ is in the far field, the gradient of the pressure and the Green's function is approximately given by

$$\nabla p(\mathbf{r}) = ik\hat{\mathbf{s}}p(\mathbf{r}) \qquad \text{and} \qquad \nabla G(\mathbf{r}, \mathbf{r}_r) = -ik\hat{\mathbf{r}}G(\mathbf{r}, \mathbf{r}_r).$$
(A-1)

As shown in Figure A-1, the unit vectors $\hat{\mathbf{s}}$ and $\hat{\mathbf{r}}$ point along the geometric ray that joins the source to $\mathbf{r}$ and along the geometric ray from $\mathbf{r}$ to the receiver, respectively. Using the far-field approximation, equation (1) can be written as

$$p(\mathbf{r}_r) = -\int_S \frac{ik}{\rho(\mathbf{r})} p(\mathbf{r})G(\mathbf{r}, \mathbf{r}_r)(\cos\theta_s + \cos\theta_r)\, dS,$$
(A-2)

where the angles θ_r and θ_s are defined in Figure A1. The factor $(\cos\theta_s + \cos\theta_r)$ is called the *obliquity factor* (Jackson, 1962).

Next, we turn to traveltime perturbation theory. Let the slowness $u(\mathbf{r})$ be perturbed with a small perturbation $\delta u(\mathbf{r})$. To first order, the wavefield $p(\mathbf{r})$ is perturbed with a perturbation $\delta p(\mathbf{r})$. There are (at least) two ways to compute the first-order perturbation in the arrival time. Luo and Schuster (1991) and Marquering et al. (1999) show that the perturbation of the traveltime computed from a crosscorrelation technique to leading

order is given by

$$\delta t = \frac{\int \dot{p}(t)\delta p(t)dt}{\int \ddot{p}(t)p(t)dt},$$
(A-3)

where the time integration is over a time window in which the wave event of interest arrives. Spetzler and Snieder (2001) show with the Rytov approximation that the traveltime shift δt is given by

$$\delta t = \omega^{-1}\Im m\left(\frac{\delta p(\omega)}{p(\omega)}\right).$$
(A-4)

With the Born approximation for the first-order perturbation of the wavefield $\delta p(\mathbf{r}_r)$ that is

$$\delta p(\mathbf{r}_r) = -\int_V 2\omega^2 p(\mathbf{r})G(\mathbf{r}, \mathbf{r}_r)u(\mathbf{r})\delta u(\mathbf{r})\, dV,$$
(A-5)

the change in traveltime can to leading order be related to the slowness perturbation through

$$\delta t = \int_V K(\mathbf{r})\delta u(\mathbf{r})\, dV.$$
(A-6)

The latter formula is again equation (6). It follows from equation (A-5) that the sensitivity kernel for travel timeshifts is proportional to $2\omega u(\mathbf{r})p(\mathbf{r})G(\mathbf{r}, \mathbf{r}_r)$ whereas the Kirchhoff integral in equation (A-2) has an integrand proportional to $(i\omega u(\mathbf{r})/\rho(\mathbf{r}))(\cos\theta_s + \theta_r)p(\mathbf{r})G(\mathbf{r}, \mathbf{r}_r)$. Apart from different multiplicative factors, which in general vary smoothly over space, the Fréchet derivative for the traveltime perturbation and the integrand of the Kirchhoff integral have the same dependence on the wavefields $p(\mathbf{r})G(\mathbf{r}, \mathbf{r}_r)$. For this reason, we use the sensitivity kernel to monitor the properties of the Fresnel zone. The advantage of using the sensitivity kernel is that it is defined over the volume of the medium, whereas the Kirchhoff integral is defined on a surface only; the sensitivity kernel in expression (A-6) thus provides information on the Fresnel zone throughout the volume.
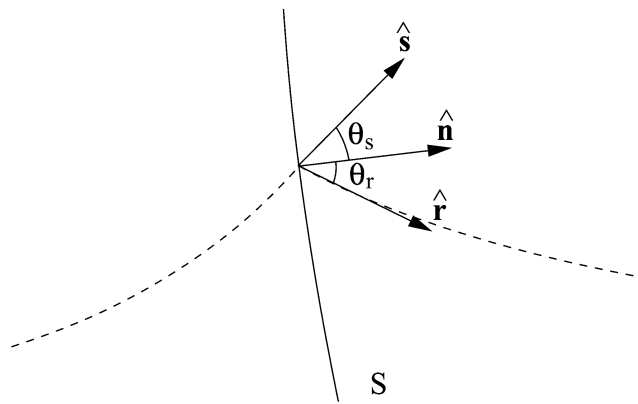

Figure A-1. Definition of the unit vectors $\hat{\mathbf{s}}$ and $\hat{\mathbf{r}}$ that point along the geometric rays indicated with dashed lines, and the angles θ_s and θ_r that these vectors make with the normal vector $\hat{\mathbf{n}}$ to the surface.

REFERENCES

Aki, K., and Richards, P. G., 1980, Quantitative seismology, theory and methods: Freeman and Co.
Aldridge, D. F., 1994, Linearization of the eikonal equation: Geophysics, **59**, 1631–1632.
Bamler, R., and Hartl, P., 1998, Synthetic aperture radar interferometry: Inverse Problems, **14**, R1-R54.
Berkhout, A. J., 1984, Seismic resolution, resolving power of acoustical echo techniques: Geophysical Press.
Červený V., 2001, Seismic ray tracing: Cambridge University Press.
Červený, V., and Soares J. E., 1992, Fresnel volume ray tracing: Geophysics, **57**, 902–915.
Claerbout, J. F., 1984, Imaging the earth's interior: Blackwell Scientific Publisher, Inc.
Chen, J., and Schuster, G. T., 1999, Resolution limits of migration images: Geophysics, **64**, 1046–1053.
Dahlen, F. A., and Baig, A. M., 2002, Fréchet kernels for body-wave amplitudes: Geophysical Journal International, **150**, 440–466.
Hubral, P., Schleicher, J., Tygel, M., and Hanitzsch, C., 1993, Determination of Fresnel zones from traveltime measurements: Geophysics, **58**, 703–712.
Jackson, J. D., 1962, Classical electrodynamics: John Wiley and Sons.
Knapp, R. W., 1991, Fresnel zones in the light of broadband data: Geophysics **56**, 354–359.
Kravtsov, Y. A., 1988, Rays and caustics as physical objects, *in* E. Wolf, ed., Progress in optics, XXVI: Elsevier, 227–348.
Luo, Y., and Schuster, G. T., 1991, Wave-equation traveltime inversion: Geophysics **56**, 645–653.
Marquering, H., Dahlen, F. A., and Nolet, G., 1999, Three-dimensional sensitivity kernels for finite-frequency traveltimes: The banana-doughnut paradox: Geophysical Journal International, **137**, 805–815.

Massonnet, D., and Feigl, K. L., 1998, Radar interferometry and its application to changes in the earth's surface: Reviews of Geophysics, **36**, 441–500.

Morse, P., and Feshbach, H., 1953, Methods of theoretical physics: McGraw-Hill.

Neele, F. P., and Snieder, R., 1992, Topography of the 400 km discontinuity from observations of long-period $P_{400}P$ phases: Geophysical Journal International, **109**, 670–682.

Nolet, G., and Dahlen, F. A., 2000, Wave front healing and the evolution of seismic delay times: Journal of Geophysical Research, **105**, 19 043–19 054.

Pratt, R. G., and Coulty, N. R., 1991, Combining wave-equation imaging with traveltime tomography to form high-resolution images from crosshole data: Geophysics, **56**, 208–224.

Pulliam, J., and Snieder, R., 1998, Ray perturbation theory, dynamic ray tracing, and the determination of Fresnel zones: Geophysical Journal International, **135**, 463–469.

Reiter, D. T., and Rodi, W., 1996, Nonlinear waveform tomography applied to crosshole seismic data: Geophysics, **61**, 902–913.

Scales, J., and Snieder, R., 1999, What is a wave?: Nature, **401**, 739–740.

Schleicher, J., Hubral, P., Tygel, M., and Jaya, M., 1997, Minimum apertures and Fresnel zones in migration and demigration: Geophysics, **62**, 183–194.

Sheriff, R. E., and Geldart, L. P., 1982, Exploration seismology, Vol. 1: History, theory and data acquisition: Cambridge University Press.

Snieder, R., 2001, A guided tour of mathematical methods for the physical sciences: Cambridge University Press.

Snieder, R., and Chapman, C., 1998, The reciprocity properties of geometrical spreading: Geophysics, **132**, 89–95.

Snieder, R., and Lomax, A., 1996, Wavefield smoothing and the effect of rough velocity perturbations on arrival times and amplitudes: Geophysical Journal International, **125**, 796–812.

Snieder, R., and Sambridge, M., 1992, Ray perturbation theory for travel times and ray paths in 3-D heterogeneous media: Geophysical Journal International, **109**, 294–322.

Spetzler, J., 2003, Comparison of ray theory and finite-frequency wave theory in crosswell tomography: 65th Meeting, European Association of Geoscientist and Engineers, Extended Abstracts, F40.

Spetzler, J., and Snieder, R., 2001, The effects of small-scale heterogeneity on the arrival time of waves: Geophysical Journal International, **145**, 786–796.

Spetzler, J., Sivaji, C., Nishizawa, O., and Fukushima, Y., 2002, A test of ray theory and scattering theory based on a laboratory experiment using ultrasonic waves and numerical simulations by finite-difference method: Geophysical Journal International, **148**, 165–178.

Stockwell, J. W., Jr., 1997, Free software in education: A case study of CWP/SU: Seismic Un*x: The Leading Edge, **16**, 1054–1059.

Tarantola, A., 1987, Inverse problem theory: Elsevier.

Wapenaar, C. P. A., and Herrmann, F. J., 1996, True-amplitude migration taking fine layering into account: Geophysics, **61**, 795-803.

Wielandt, E., 1987, On the validity of the ray approximation for interpreting delay times, *in* G. Nolet, ed., Seismic tomography: Reidel, 85–98.

Williamson, P. R., 1991, A guide to the limits of resolution imposed by scattering in ray tomography: Geophysics, **56**, 202–207.

Williamson, P. R., and Worthington, M. H., 1993, Resolution limits in ray tomography due to wave behavior: Numerical experiments: Geophysics, **58**, 727–735.

Woodward, M. J., 1992, Wave-equation tomography: Geophysics, **57**, 15–26.

Yilmaz, Ö., 1987, Seismic data processing: SEG.

Yomogida, K., and Aki, K., 1987, Amplitude and phase data inversions for phase velocity anomalies in the Pacific Ocean basin: Geophysical Journal of the Royal Astronomical Society, **88**, 161–204.